Thermalization of a spin chain strongly coupled to its environment

Gerald E. Fux,[1] Dainius Kilda,[2] Brendon W. Lovett,[1] and Jonathan Keeling[1]

[1] *SUPA, School of Physics and Astronomy, University of St Andrews, St Andrews, KY16 9SS, United Kingdom*
[2] *Max-Planck-Institut für Quantenoptik, Hans-Kopfermann-Str. 1, D-85748 Garching, Germany*

(Dated: January 17, 2022)

We study the thermalization of individual spins of a short XYZ Heisenberg chain with strongly coupled thermal leads by checking the consistency of two-time correlations with the fluctuation-dissipation theorem. To compute these correlations we develop and apply a general numerical method for chains of quantum systems, where each system may couple strongly to a structured environment. The method combines the process tensor formalism for general (possibly non-Markovian) open quantum systems with time evolving block decimation for 1D chains. It systematically reduces the numerical complexity originating from system-environment correlations before integrating them into the full many-body problem, making a wide range of applications numerically feasible. Our results show the complete thermalization of the chain when coupled to a single bath, and reveal distinct effective temperatures in low, mid, and high frequency regimes when placed between a hot and a cold bath.

When studying many-body quantum systems a natural question arising is whether a particular subsystem has thermalized. Identifying that a subsystem is in thermal equilibrium allows one to link its microscopic state to thermodynamic properties and simplifies its description [1]. Answering this question is especially interesting—and also particularly challenging—for non-equilibrium steady states of many-body systems that are coupled strongly to thermal baths [2–6]. Such scenarios are of importance for fundamental research, such as the study of strong coupling quantum thermodynamics [7–12], as well as technological and biological applications [13–19].

A popular approach to the study of thermalization of a subsystem is based on obtaining its reduced density matrix [20–24]. The reduced density matrix is, however, only a small fraction of the operationally accessible information of an open system. In many experiments the observed quantities are related to multi-time correlations, as are for instance the fluorescence and absorption spectra in molecular spectroscopy, and bunching and anti-bunching of photons in quantum optics experiments. We thus propose to use this additional information to check whether the two-time correlations of a subsystem are consistent with thermal equilibrium. For this we check whether the fluctuation and dissipation spectra of an observable of the subsystem in question obey the fluctuation-dissipation theorem (FDT).

The FDT states that for a thermalized quantum system at temperature T the ratio of the fluctuation and dissipation spectra with respect to any observable $\hat{A}$ must be $S_A(\omega)/\chi''_A(\omega) = \coth\left(\frac{\omega}{2T}\right)$ [25, 26]. The fluctuation spectrum $S_A(\omega)$, also known as the symmetrized quantum noise spectral density [27], is the Fourier transform of the Keldysh Green's function $S_A(\tau) = \frac{1}{2}\langle\{\hat{A}(\tau), \hat{A}(0)\}\rangle$. Similarly, the dissipation spectrum $\chi''_A(\omega)$ is the imaginary part of the Fourier transformed linear response function $\chi_A(\tau) = i\Theta(\tau)\langle[\hat{A}(\tau), \hat{A}(0)]\rangle$ and quantifies the density of states with respect to transitions driven by the operator $\hat{A}$. Together, the fluctuation and dissipation spectra carry information about the energy levels and their occupation, allowing an assessment of whether the system has thermalized. Any thermometer measures the temperature, not of an entire system, but of the degree of freedom to which it couples. Checking the FDT for a particular observable corresponds to weakly coupling a thermometer to that part of the system.

It is important to note that the most commonly applied approaches for open quantum systems, such as the time-convolutionless, Nakajima-Zwanzig, and Gorini–Kossakowski–Sudarshan–Lindblad (GKSL) master equations [28], aim at correctly describing the reduced system dynamics, but are in general unsuitable for obtaining correct multi-time correlations. Consider, for example, even just a single two-level system coupled to a thermal bath: a secularized Born-Markov master equation can lead to the correct thermal Gibbs state in a weak coupling limit, but yields two-time correlations which are inconsistent with the FDT [29, 30]. This is because for master equation approaches one needs to invoke the so called "quantum regression theorem" [31] which itself relies on the Born approximation. Particularly interesting scenarios, however, involve strong coupling to both the neighboring parts of a many-body system as well as the continuous set of modes of a thermal bath. In such cases, correlations between the system and environment play an important role for the correct computation of the two-time correlations but cannot be encoded in the reduced density matrix alone. In order to use the FDT to judge the temperature of a subsystem, it is therefore necessary to have access to a method that can correctly compute multi-time correlations of many-body open quantum systems.

In this Letter we study a short XYZ Heisenberg spin chain with strongly coupled leads at different temperatures and determine to what extent one can assign a

temperature to the individual spins in the steady state. To study such a scenario we present a general numerical method that augments time evolving block decimation (TEBD) [32–35] with the process tensor formalism [36]. This method enables the computation of multi-time correlations of chains of non-Markovian open quantum systems. As discussed below, it is based on a representation of the process tensor in a matrix product operator form (PT-MPO) which encodes the complex system-environment correlations and allows to compress the influence of the environment to capture the most physically relevant sector of the exponentially large parameter space [37–43]. Utilizing this method we first demonstrate the (expected) complete thermalization for coupling to a single bath and contrast this to the failure of a widely-used approximate approach. For two baths at different temperatures, we can define a frequency dependent effective temperature $T(\omega)$ and identify different behavior in low, mid, and high frequency regimes.

Process tensors and TEBD.—We start by presenting a general numerical tensor network method to study multi-time correlations of chains of open quantum systems. Each system may individually couple strongly to a structured environment. The spin chain with strongly coupled thermal leads, which we will study subsequently, is a special case of such a setup, where only the first and the last site of the chain are coupled to an environment (see Fig. 1d). The method is applicable to a wide variety of different environments such as boson, fermion, and spin baths. The only restriction on the environments is that the associated PT-MPO can be efficiently constructed. The PT-MPO is based on the process tensor formalism which is a general operational approach

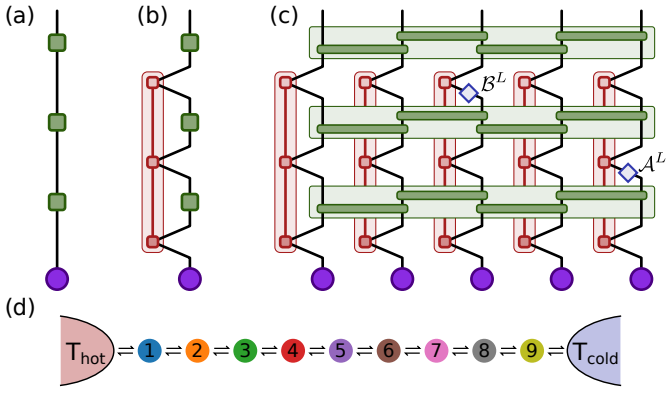

FIG. 1. Tensor networks for the simulation of a single closed (a), a single open (b), and a chain of open quantum systems (c). The purple circles and green squares represent the initial system states and the system propagators. The red and green shaded areas highlight the PT-MPOs and the TEBD propagators. In panel (c) the super-operators $\mathcal{A}^L$ and $\mathcal{B}^L$ are inserted to calculate the two-time correlation $\langle \hat{B}_3(2\,\delta t)\hat{A}_5(1\,\delta t)\rangle$. Panel (d) shows a sketch of the 9-site spin chain coupled to two thermal baths at different temperatures.

to non-Markovian open quantum systems. Its central object—the process tensor (PT) [36]—is a multi linear map from the set of all possible system control operation sequences to the resulting output states. It allows the computation of any multi-time correlation function of the system by inserting control operations at the respective times. The PT exists for *any* environment and is also called the quantum comb [44], (generalized) influence functional [37, 42], and process matrix [45]. Generically it is a high rank tensor that grows exponentially with the number of time steps. In many cases, however, it is possible to systematically discard negligible correlations and express the PT as a tensor network [46] in a matrix product operator (MPO) form [47], allowing a numerically efficient representation. For different environments different methods for the construction of a PT-MPO exist. For linearly coupled Gaussian bosonic environments one can directly construct a tensor network that yields a PT-MPO [37–40]. Other approaches [41, 42] allow the construction of PT-MPOs for any environment that can be approximated by a finite set of independent degrees of freedom. It is also possible to construct PT-MPOs directly from experimental measurements [43].

The tensor network we propose for a chain of open quantum systems is presented in Fig. 1c and can best be understood by first considering the simpler tensor networks for a single closed (Fig. 1a) and a single open quantum system (Fig. 1b). The purple circle with one leg in Fig. 1a represents the vectorized initial density matrix of the system. The green boxes with two legs represent the propagator matrices $\mathcal{U}^S = \exp\left(\mathcal{L}^S \delta t\right)$ in Liouville space for a short time step δt, where $\mathcal{L}^S = -i[\hat{H}^S, \cdot]$ is the system Liouvillian associated with the system Hamiltonian $\hat{H}^S$. The entire diagram in Fig. 1a has one unconnected leg and thus represents a vector, namely the vectorized system density matrix after three time steps.

Figure 1b shows the tensor network for the evolution of a single *open* quantum system. The red dashed region contains a PT-MPO obtained by one of the methods mentioned above. This tensor network relies on a Suzuki-Trotter expansion of the total propagator $e^{-i\hat{H}\delta t}$ into propagators $e^{-i\hat{H}^S\delta t}\, e^{-i\hat{H}^E\delta t}$ of the pure system part $\hat{H}^S$ and the remainder $\hat{H}^E$, plus higher order terms $\mathcal{O}(\delta t^2)$. The time step δt must be chosen small enough such that these higher-order terms can be neglected. The entire tensor network represents the vectorized system density matrix after three time steps taking the environment influence into account.

Figure 1c shows the proposed tensor network for the simulation of a chain of system-environment pairs, which is a combination of the network shown in Fig. 1b with TEBD in Liouville space [34, 35]. We assume a total Hamiltonian of the form

$$\hat{H} = \sum_{n=1}^{N} \left(\hat{H}_n^S + \hat{H}_n^E\right) + \sum_{n=1}^{N-1} \hat{K}_{n,n+1}, \qquad (1)$$

with N system-environment pairs and nearest neighbor couplings $\hat{K}_{n,n+1}$ among the systems. For each system, the complex interaction with its environment is encoded in a PT-MPO (the red shaded areas). The green shaded areas represent the propagation of the closed system chain for short time steps δt. For ease of presentation Fig. 1c shows the tensor network for the propagation of the closed chain in a first-order Suzuki-Trotter splitting among the chain sites, but higher order expansions are also possible. Here, the time step needs to be chosen small enough such that the Suzuki-Trotter expansion of the evolution is valid for both the system-environment and the internal system-system coupling terms. Also for ease of presentation, the tensor network shown in Fig. 1c is restricted to uncorrelated initial states. We present the full tensor network for a second-order Suzuki-Trotter expansion and correlated initial states in the supplemental material (SM) [48]. For a Markovian environment (for which the internal legs of the process tensor disappear [49]) this tensor network reduces to a TEBD network in Liouville space. This method is also related to an approach introduced by Bañuls *et al.* [50, 51] to study a subsystem of an infinite chain by contracting a conventional TEBD network in the spatial direction, which can be understood as the construction of a PT-MPO. Turning back to Fig. 1c, the two additional blue diamond shaped matrices show how a tensor network of this form can be used to extract multi-time correlations such as $\langle \hat{B}_m(t_2)\hat{A}_n(t_1)\rangle$ for arbitrary system operators $\hat{A}$, $\hat{B}$ at sites n, m, and times t_1, t_2 respectively. For this, we multiply the system propagators with the left acting superoperators $\mathcal{A}^L(\rho) = \hat{A}\rho$ at time step t_1 and $\mathcal{B}^L$ at time step t_2.

We note that alternative numerical methods to compute the dynamics of chains of sites coupled to individual environments exist [52–59]. A method proposed by Suzuki *et al.* [54] is based on the transfer matrix approach and restricted to Gaussian bosonic environments as well as diagonal system-system couplings (with respect to the local system basis). The modular path integral (MPI) method [53] is originally based on the same assumptions, but has recently been extended to more general cases [56, 57]. Another recently introduced approach is based on a quantum state diffusion method, also assuming Gaussian bosonic environments [58]. Very recently Bose and Walters proposed a multi-site decomposition of the tensor network path integral (MS-TNPI) [59], which is similar to the method presented in this Letter, but again restricted to Gaussian bosonic environments and comparatively short memory times (only 4 time steps are presented). In the special case where only the end sites couple to baths, methods such as Time Evolving Density matrices using Orthogonal Polynomials (TEDOPA) can be used, where the baths are mapped to extended chains [60–62]. These alternative approaches attempt to tackle the numerical complexity of both the system-system and the system-environment correlations simultaneously. In contrast to that, the PT-MPO approach tackles these challenges sequentially by first systematically reducing the numerical complexity originating from system-environment correlations before integrating them into the full many-body problem. This enables us to tackle a much broader class of problems.

An XYZ spin chain with thermal leads.—With this numerical method at hand we can now turn to the study of an XYZ chain with strongly coupled thermal leads. We consider the chain Hamiltonian

$$\hat{H}_{\mathrm{XYZ}} = \sum_{n=1}^{N} \epsilon_n \hat{s}_n^z + \sum_{n=1}^{N-1} \sum_{\gamma\in\{x,y,z\}} J^\gamma \, \hat{s}_n^\gamma \hat{s}_{n+1}^\gamma, \qquad (2)$$

where $\hat{s}_n^\gamma = \hat{\sigma}_n^\gamma/2$ denote the spin-1/2 operators at site n. We choose $J^x = 1.3$, $J^y = 0.7$, and $J^z = 1.2$ to break the symmetries of the Heisenberg model, and start with homogeneous on-site energies $\epsilon_n = 1$. We set $\hbar = k_\mathrm{B} = 1$ and express all frequencies and times in units of some characteristic frequency and its inverse.

As a first check we couple a single bath at temperature $T = 1.6$ to only the first site of a short ($N = 5$) chain. We aim to confirm that at the steady state each spin has come to thermal equilibrium at temperature T. The bath couples to the chain operator $\hat{s}_1^y$ with

$$\hat{H}_1^E = \sum_{k=0}^{\infty} \left[\hat{s}_1^y \left(g_k \hat{b}_k^\dagger + g_k^* \hat{b}_k \right) + \omega_k \hat{b}_k^\dagger \hat{b}_k \right], \qquad (3)$$

where $\hat{b}_k^{(\dagger)}$ are bosonic lowering (raising) bath operators. The g_k parameters are determined by the spectral density $J(\omega) = \sum_k |g_k|^2 \delta(\omega - \omega_k)$ which we choose to take

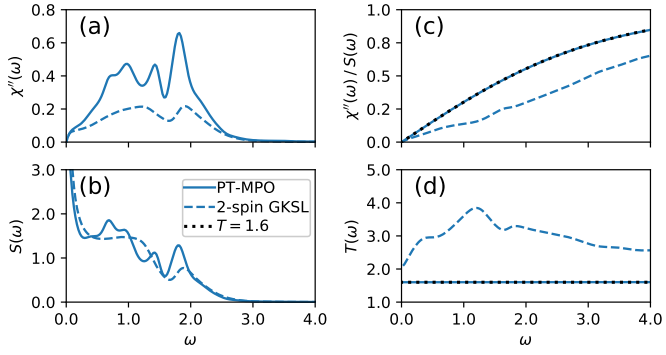

FIG. 2. Two-time correlations of the steady state for the $\hat{\sigma}^z$ observable of the middle spin in a 5-site chain coupled to a single bath at temperature $T = 1.6$. The solid and dashed lines show the results obtained employing the PT-MPO approach and a 2-spin driving protocol [63–65], respectively. The panels show the dissipation spectrum (a), the fluctuation spectrum (b), their ratio (c), and the corresponding effective temperature (d). The PT-MPO results overlap with the expected FDT $\tanh(\frac{\omega}{2T})$ (dotted line) in (c) and show no frequency dependence in (d), confirming complete thermalization.

the form $J(\omega) = 2\alpha\omega \exp(-\omega/\omega_c)$. We use a coupling strength $\alpha = 0.32$ and cutoff frequency $\omega_c = 4.0$. Perturbation theory predicts that in a weak coupling limit, $\alpha \to 0$, the reduced chain density matrix of the full thermal state differs from the Gibbs state of the chain Hamiltonian at a quadratic order in the bath coupling [24]. We confirm this and present the results in the SM [48].

Figure 2 shows the simulation results for the fluctuation and dissipation spectra for the $\hat{\sigma}^z$ observable of the middle spin in the chain. The solid lines show the results obtained using the PT-MPO technique (for the details of the numerical simulation see the SM [48]). Figure 2c shows the ratio of the dissipation and fluctuation spectra, which has the shape of a hyperbolic tangent. Inverting the fluctuation-dissipation theorem and plotting a frequency dependent effective temperature $T(\omega) = \omega/[2\,\mathrm{artanh}(\chi''(\omega)/S'(\omega)]$ in Fig. 2d we can see from the perfectly flat line that the spin has thermalized completely at the expected temperature. We find similar results for all other spins and observables, and no dependency on the chosen initial chain state.

Figure 2 also shows the results of a different, widely applied numerical method to study thermodynamic properties of spin chains [63–65]. In this approach, two additional spins are attached to the end of the chain and driven towards their local two-spin thermal Gibbs state with a time local master equation of GKSL form in the hope that this will thermalize the rest of the chain. The two-time correlations obtained using this method strongly deviate from the FDT and are thus incorrect.

We now turn to an XYZ spin chain of length $N = 9$ coupled to two thermal leads at different temperatures. Using the PT-MPO method we couple one bath at temperature $T_{\mathrm{hot}} = 1.6$ to the first spin and one bath at $T_{\mathrm{cold}} = 0.8$ to the last spin (see Fig. 1d), using the same spectral density and method as before. Figures 3a and 3b show the dissipation spectrum $\chi''(\omega)$ and the effective temperature $T(\omega)$ for the $\hat{\sigma}^z$ observable of each spin.

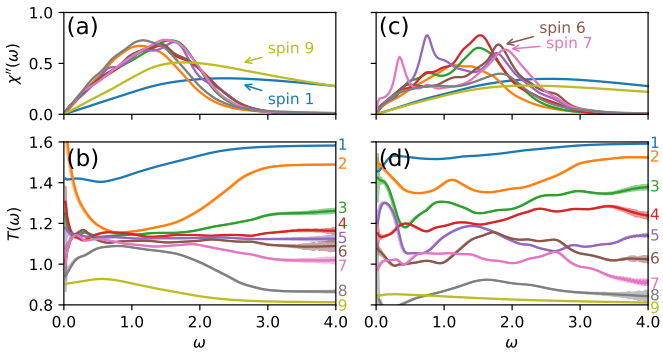

FIG. 3. The dissipation spectrum (a) and effective temperature (b) at steady state for the σ^z observable of each spin in a 9-site spin chain placed between a hot ($T_{\mathrm{hot}} = 1.6$) and cold bath ($T_{\mathrm{cold}} = 0.8$). Panels (c) and (d) show the results for the same chain with additional on-site disorder $\epsilon_n = 1 + x_n$, for a random draw of x_n from a uniform distribution in $(-1.6, 1.6)$. The shaded regions in panel (b) and (d) show an estimate of the numerical error.

In Fig. 3b we observe that at a mid frequency range (between roughly 0.5 and 2.0) the inner spins adopt a common intermediate effective temperature, while at higher frequencies (above approximately 3.0) each spin adopts an effective temperature between that of the hot and cold bath depending on its position. In the following we suggest an idea for why this kind of behavior might arise. We first consider the eigenstates of the closed XYZ spin chain, which consist of a set of delocalized "bulk" states and localized "surface" states. The surface states are mainly localized each at one end of the chain, but reach into the bulk with an exponentially decaying tail. For the chain parameters chosen here the density of states for the closed spin chain slowly vanishes above a frequency of approximately 2.5 (see the SM [48]). In the mid frequency range the density of states for the inner spins is dominated by the bulk states. When we include the coupling to the environments, the bulk states hybridize weakly with both environments due to their equal and small overlap with the two outer spins, which leads to the intermediate common temperature of the inner spins. For the higher frequencies, however, the density of states is dominated by the surface states. This is because the surface states have a large overlap with either the first or last spin and thus hybridize strongly with the left or right environment respectively. Because the coupling of a spin with the left and right surface states strongly depends on its position, the effective temperature it adopts depends on its position as well.

This picture is also consistent with the dissipation spectrum plotted in Fig. 3a, showing different behavior for the inner and outer spins. Furthermore, we can verify this interpretation of our results by adding random on-site disorder and observing that the formation of localized modes destroys the collective common temperature at mid frequencies as expected (see Fig. 3c and 3d). Finally, we note that the low frequency limit effective temperatures in Figs. 3b and 3d are drastically different from the effective temperatures at mid and higher frequencies. This suggests limitations to the significance of the low-frequency effective temperature [66, 67], because it captures only a very small fraction of excitations in the system adequately.

Conclusion—We have presented a numerical method for computing multi-time correlations of many-body quantum systems in the presence of strongly coupled and structured environments and have demonstrated that two-time correlations can be used to study thermalization of subsystems. A key ingredient of this method is the PT-MPO which encodes the influence of the environment and reduces it to the most physically relevant sector of the parameter space. Compressing the environment influence before tackling the full many-body prob-

lem greatly reduces the effective dimension of the computation and makes the simulation of a large class of many-body open quantum systems numerically feasible. Finally, we note that the PT-MPO approach can be applied to various other many-body tensor network methods [68–72] and that it can be modified to compute full-counting statistics of heat transfer [73]. It thus enables the development of a versatile set of numerical tools to study dynamics, correlations, and thermodynamic properties of many-body open quantum systems.

G.E.F. and D.K. acknowledge support from EPSRC (EP/L015110/1). B.W.L. and J.K. acknowledge support from EPSRC (EP/T014032/1).

[1] W. Greiner, L. Neise, and H. Stöcker, *Thermodynamics and statistical mechanics* (Springer Science & Business Media, 2012).

[2] Y. Blanter and M. Büttiker, Shot noise in mesoscopic conductors, Phys. Rep. **336**, 1 (2000).

[3] N. Agraït, A. L. Yeyati, and J. M. van Ruitenbeek, Quantum properties of atomic-sized conductors, Phys. Rep. **377**, 81 (2003).

[4] F. Giazotto, T. T. Heikkilä, A. Luukanen, A. M. Savin, and J. P. Pekola, Opportunities for mesoscopics in thermometry and refrigeration: Physics and applications, Rev. Mod. Phys. **78**, 217 (2006).

[5] M. D. Losego, M. E. Grady, N. R. Sottos, D. G. Cahill, and P. V. Braun, Effects of chemical bonding on heat transport across interfaces, Nat. Mater. **11**, 502 (2012).

[6] J. R. Widawsky, W. Chen, H. Vázquez, T. Kim, R. Breslow, M. S. Hybertsen, and L. Venkataraman, Length-Dependent Thermopower of Highly Conducting Au–C Bonded Single Molecule Junctions, Nano Lett. **13**, 2889 (2013).

[7] L. Nicolin and D. Segal, Quantum fluctuation theorem for heat exchange in the strong coupling regime, Phys. Rev. B **84**, 161414(R) (2011).

[8] M. Horodecki and J. Oppenheim, Fundamental limitations for quantum and nanoscale thermodynamics, Nat. Commun. **4**, 2059 (2013).

[9] S. Vinjanampathy and J. Anders, Quantum thermodynamics, Contemp. Phys. **57**, 545 (2016).

[10] U. Seifert, First and second law of thermodynamics at strong coupling, Phys. Rev. Lett. **116**, 020601 (2016).

[11] F. Binder, L. A. Correa, C. Gogolin, J. Anders, and G. Adesso, *Thermodynamics in the quantum regime: fundamental aspects and new directions*, Vol. 195 (Springer, 2019).

[12] P. Talkner and P. Hänggi, Colloquium: Statistical mechanics and thermodynamics at strong coupling: Quantum and classical, Rev. Mod. Phys. **92**, 041002 (2020).

[13] S. Bose, Quantum communication through an unmodulated spin chain, Phys. Rev. Lett. **91**, 207901 (2003).

[14] A. Wójcik, T. Łuczak, P. Kurzyński, A. Grudka, T. Gdala, and M. Bednarska, Unmodulated spin chains as universal quantum wires, Phys. Rev. A **72**, 034303 (2005).

[15] G. S. Engel, T. R. Calhoun, E. L. Read, T. K. Ahn, T. Mančal, Y. C. Cheng, R. E. Blankenship, and G. R. Fleming, Evidence for wavelike energy transfer through quantum coherence in photosynthetic systems, Nature **446**, 782 (2007).

[16] N. Lambert, Y. N. Chen, Y. C. Cheng, C. M. Li, G. Y. Chen, and F. Nori, Quantum biology, Nat. Phys. **9**, 10 (2013).

[17] H. N. Motlagh, J. O. Wrabl, J. Li, and V. J. Hilser, The ensemble nature of allostery, Nature **508**, 331 (2014).

[18] M. T. Mitchison, Quantum thermal absorption machines: refrigerators, engines and clocks, Contemp. Phys. **60**, 164 (2019).

[19] J. Cao, R. J. Cogdell, D. F. Coker, H.-G. Duan, J. Hauer, U. Kleinekathöfer, T. L. C. Jansen, T. Mančal, R. J. D. Miller, J. P. Ogilvie, V. I. Prokhorenko, T. Renger, H.-S. Tan, R. Tempelaar, M. Thorwart, E. Thyrhaug, S. Westenhoff, and D. Zigmantas, Quantum biology revisited, Sci. Adv. **6**, eaaz4888 (2020).

[20] C. Jarzynski, Nonequilibrium work theorem for a system strongly coupled to a thermal environment, J. Stat. Mech. Theory Exp. **2004**, P09005 (2004).

[21] M. Campisi, P. Talkner, and P. Hänggi, Fluctuation theorem for arbitrary open quantum systems, Phys. Rev. Lett. **102**, 210401 (2009).

[22] Y. Subaşı, C. H. Fleming, J. M. Taylor, and B. L. Hu, Equilibrium states of open quantum systems in the strong coupling regime, Phys. Rev. E **86**, 061132 (2012).

[23] M. Perarnau-Llobet, H. Wilming, A. Riera, R. Gallego, and J. Eisert, Strong coupling corrections in quantum thermodynamics, Phys. Rev. Lett. **120**, 120602 (2018).

[24] A. S. Trushechkin, M. Merkli, J. D. Cresser, and J. Anders, Open quantum system dynamics and the mean force Gibbs state, (2021), arXiv:2110.01671.

[25] R. Kubo, The fluctuation-dissipation theorem, Rep. Prog. Phys. **29**, 255 (1966).

[26] R. Kubo, M. Toda, and N. Hashitsume, *Statistical Physics II: Nonequilibrium Statistical Mechanics* (Springer, 1978).

[27] A. A. Clerk, M. H. Devoret, S. M. Girvin, F. Marquardt, and R. J. Schoelkopf, Introduction to quantum noise, measurement, and amplification, Rev. Mod. Phys. **82**, 1155 (2010).

[28] H.-P. Breuer and F. Petruccione, *The Theory of Open Quantum Systems* (Oxford University Press, 2002).

[29] G. W. Ford and R. F. O'Connell, There is no quantum regression theorem, Phys. Rev. Lett. **77**, 798 (1996).

[30] G. Guarnieri, A. Smirne, and B. Vacchini, Quantum regression theorem and non-markovianity of quantum dynamics, Phys. Rev. A **90**, 022110 (2014).

[31] M. Lax, Formal theory of quantum fluctuations from a driven state, Phys. Rev. **129**, 2342 (1963).

[32] G. Vidal, Efficient classical simulation of slightly entangled quantum computations, Phys. Rev. Lett. **91**, 147902 (2003).

[33] G. Vidal, Efficient simulation of one-dimensional quantum many-body systems, Phys. Rev. Lett. **93**, 040502 (2004).

[34] A. J. Daley, C. Kollath, U. Schollwöck, and G. Vidal, Time-dependent density-matrix renormalization-group using adaptive effective hilbert spaces, J. Stat. Mech. Theory Exp. **2004**, P04005 (2004).

[35] M. Zwolak and G. Vidal, Mixed-state dynamics in one-dimensional quantum lattice systems: A time-dependent superoperator renormalization algorithm, Phys. Rev. Lett. **93**, 207205 (2004).

[36] F. A. Pollock, C. Rodríguez-Rosario, T. Frauenheim, M. Paternostro, and K. Modi, Non-markovian quantum processes: Complete framework and efficient characterization, Phys. Rev. A **97**, 012127 (2018).

[37] M. R. Jørgensen and F. A. Pollock, Exploiting the causal tensor network structure of quantum processes to efficiently simulate non-markovian path integrals, Phys. Rev. Lett. **123**, 240602 (2019).

[38] A. Strathearn, *Modelling Non-Markovian Quantum Systems Using Tensor Networks*, Springer Theses (Springer International Publishing, Cham, 2020).

[39] G. E. Fux, E. P. Butler, P. R. Eastham, B. W. Lovett, and J. Keeling, Efficient exploration of hamiltonian parameter space for optimal control of non-markovian open quantum systems, Phys. Rev. Lett. **126**, 200401 (2021).

[40] The TEMPO collaboration, TimeEvolvingMPO: A Python 3 package to efficiently compute non-Markovian open quantum systems. (2020).

[41] M. Cygorek, M. Cosacchi, A. Vagov, V. M. Axt, B. W. Lovett, J. Keeling, and E. M. Gauger, Numerically exact open quantum systems simulations for arbitrary environments using automated compression of environments, (2021), arXiv:2101.01653.

[42] E. Ye and G. K.-L. Chan, Constructing tensor network influence functionals for general quantum dynamics, J. Chem. Phys. **155**, 044104 (2021).

[43] G. A. L. White, F. A. Pollock, L. C. L. Hollenberg, K. Modi, and C. D. Hill, Non-Markovian Quantum Process Tomography, (2021), arXiv:2106.11722.

[44] G. Chiribella, G. M. D'Ariano, and P. Perinotti, Quantum circuit architecture, Phys. Rev. Lett. **101**, 060401 (2008).

[45] O. Oreshkov, F. Costa, and Č. Brukner, Quantum correlations with no causal order, Nat. Commun. **3**, 1092 (2012).

[46] R. Orús, A practical introduction to tensor networks: Matrix product states and projected entangled pair states, Ann. Phys. (N. Y.) **349**, 117 (2014).

[47] F. Verstraete, J. J. García-Ripoll, and J. I. Cirac, Matrix product density operators: Simulation of finite-temperature and dissipative systems, Phys. Rev. Lett. **93**, 207204 (2004).

[48] See Supplemental Material attached to this manuscirpt for details on: the PT augmented TEBD tensor network and the XYZ spin chain simulations.

[49] F. A. Pollock, C. Rodríguez-Rosario, T. Frauenheim, M. Paternostro, and K. Modi, Operational markov condition for quantum processes, Phys. Rev. Lett. **120**, 040405 (2018).

[50] M. C. Bañuls, M. B. Hastings, F. Verstraete, and J. I. Cirac, Matrix product states for dynamical simulation of infinite chains, Phys. Rev. Lett. **102**, 240603 (2009).

[51] A. Müller-Hermes, J. I. Cirac, and M. C. Bañuls, Tensor network techniques for the computation of dynamical observables in one-dimensional quantum spin systems, New J. Phys. **14**, 075003 (2012).

[52] N. Makri, Communication: Modular path integral: Quantum dynamics via sequential necklace linking, J. Chem. Phys. **148**, 101101 (2018).

[53] N. Makri, Modular path integral methodology for real-time quantum dynamics, J. Chem. Phys. **149**, 214108 (2018).

[54] S. Suzuki, H. Oshiyama, and N. Shibata, Quantum annealing of pure and random ising chains coupled to a bosonic environment, J. Phys. Soc. Japan **88**, 061003 (2019).

[55] N. Makri, Small matrix modular path integral: iterative quantum dynamics in space and time, Phys. Chem. Chem. Phys. **23**, 12537 (2021).

[56] S. Kundu and N. Makri, Efficient matrix factorisation of the modular path integral for extended systems, Mol. Phys. **119**, e1797200 (2021).

[57] S. Kundu and N. Makri, Exciton-Vibration Dynamics in J-Aggregates of a Perylene Bisimide from Real-Time Path Integral Calculations, J. Phys. Chem. **125**, 201 (2021).

[58] S. Flannigan, F. Damanet, and A. J. Daley, Many-body quantum state diffusion for non-Markovian dynamics in strongly interacting systems, (2021), arXiv:2108.06224.

[59] A. Bose and P. L. Walters, A Multisite Decomposition of the Tensor Network Path Integrals, (2021), arXiv:2109.09723.

[60] J. Prior, A. W. Chin, S. F. Huelga, and M. B. Plenio, Efficient simulation of strong system-environment interactions, Phys. Rev. Lett. **105**, 050404 (2010).

[61] A. W. Chin, Á. Rivas, S. F. Huelga, and M. B. Plenio, Exact mapping between system-reservoir quantum models and semi-infinite discrete chains using orthogonal polynomials, J. Math. Phys. **51**, 092109 (2010).

[62] A. Purkayastha, G. Guarnieri, S. Campbell, J. Prior, and J. Goold, Periodically refreshed baths to simulate open quantum many-body dynamics, Phys. Rev. B **104**, 045417 (2021).

[63] T. Prosen, Matrix product simulations of non-equilibrium steady states of quantum spin chains, J. Stat. Mech. Theory Exp. **2009**, P02035 (2009).

[64] M. Žnidarič, T. Prosen, G. Benenti, G. Casati, and D. Rossini, Thermalization and ergodicity in one-dimensional many-body open quantum systems, Phys. Rev. E **81**, 051135 (2010).

[65] T. Prosen, Exact nonequilibrium steady state of a strongly driven open xxz chain, Phys. Rev. Lett. **107**, 137201 (2011).

[66] E. G. D. Torre, S. Diehl, M. D. Lukin, S. Sachdev, and P. Strack, Keldysh approach for nonequilibrium phase transitions in quantum optics: Beyond the dicke model in optical cavities, Phys. Rev. A **87**, 023831 (2013).

[67] L. M. Sieberer, M. Buchhold, and S. Diehl, Keldysh field theory for driven open quantum systems, Rep. Prog. Phys. **79**, 096001 (2016).

[68] F. Verstraete and J. I. Cirac, Renormalization algorithms for Quantum-Many Body Systems in two and higher dimensions, (2004), arXiv:0407066.

[69] G. Vidal, Classical simulation of infinite-size quantum lattice systems in one spatial dimension, Phys. Rev. Lett. **98**, 070201 (2007).

[70] R. Orús and G. Vidal, Infinite time-evolving block decimation algorithm beyond unitary evolution, Phys. Rev. B **78**, 155117 (2008).

[71] V. Murg, F. Verstraete, O. Legeza, and R. M. Noack, Simulating strongly correlated quantum systems with tree tensor networks, Phys. Rev. B **82**, 205105 (2010).

[72] M. P. Zaletel, R. S. K. Mong, C. Karrasch, J. E. Moore, and F. Pollmann, Time-evolving a matrix product state with long-ranged interactions, Phys. Rev. B **91**, 165112 (2015).

[73] M. Popovic, M. T. Mitchison, A. Strathearn, B. W.

Lovett, J. Goold, and P. R. Eastham, Quantum heat statistics with time-evolving matrix product operators, PRX Quantum **2**, 020338 (2021).

[74] M. Suzuki, General theory of higher-order decomposition of exponential operators and symplectic integrators, Phys. Lett. A **165**, 387 (1992).

SUPPLEMENTAL MATERIAL

Process tensors and TEBD

In this section we present details of our numerical method, that combines the process tensor approach to open quantum systems with time evolving block decimation (TEBD). This method allows us to compute multi-time correlations of 1D many-body quantum systems in the presence of strongly coupled and structured environments. We assume a total Hamiltonian of the form

$$\hat{H} = \sum_{n=1}^{N} \left(\hat{H}_n^S + \hat{H}_n^E \right) + \sum_{n=1}^{N-1} \hat{K}_{n,n+1}. \tag{S1}$$

It consists of on-site system Hamiltonians $\hat{H}_n^S$, on-site system-environment interaction parts $\hat{H}_n^E$, and nearest neighbor coupling terms $\hat{K}_{n,n+1}$ for each of the N sites. Formally, we require each of these operators to be in the set of bounded linear operators $\mathcal{B}(\mathcal{H})$ on the appropriate Hilbert space $\mathcal{H}$. If $\mathcal{H}_n^S$ and $\mathcal{H}_n^E$ denote the system and environment Hilbert spaces of the n^{th} site, then $\hat{H}_n^S \in \mathcal{B}(\mathcal{H}_n^S)$, $\hat{H}_n^E \in \mathcal{B}(\mathcal{H}_n^S \otimes \mathcal{H}_n^E)$, and $\hat{K}_{n,n+1} \in \mathcal{B}(\mathcal{H}_n^S \otimes \mathcal{H}_{n+1}^S)$.

In principle the on-site system Hamiltonians can be completely absorbed in the definition of the on-site system-environment interactions. However, we will see below that it is often useful to separate the pure system part from the interaction part as much as possible. In addition to the total Hamiltonian in Eq. (S1), we will also allow for on-site time-local dissipative processes described by a local master equation of GKSL form.

In the following we derive the construction of the TEBD tensor network augmented with the process tensor approach and present a suitable contraction algorithm. Finally, we will show how to extract the intermediate time chain dynamics as well as multi-site multi-time correlations.

Tensor network construction.—The entire following calculation is carried out in Liouville space, i.e. we consider super-operators that act on the space of vectorized density matrices. As a start we consider the formal solution of the von Neumann equation for the total density operator at time t

$$\rho(t) = e^{\mathcal{L}t}\rho(0) \tag{S2}$$

with the total Liouvillian $\mathcal{L} = -i[\hat{H}, \cdot]$. We can separate the total Liouvillian into a chain and environment part

$$\mathcal{L} = \mathcal{L}_{\text{chain}} + \sum_{n=1}^{N} \mathcal{L}_n^E, \tag{S3}$$

where

$$\mathcal{L}_{\text{chain}} = \sum_{n=1}^{N} \mathcal{L}_n^S + \sum_{n=1}^{N-1} \mathcal{L}_{n,n+1}^K, \tag{S4}$$

with each Liouvillian corresponding to a part of the total Hamiltonian. As mentioned above, the system Liouvillians may additionally include dissipative terms, i.e.

$$\mathcal{L}_n^S \cdot = -i[\hat{H}_n^S, \cdot] + \sum_k \left(\hat{L}_{n,k}^\dagger \cdot \hat{L}_{n,k} - \frac{1}{2}\{\hat{L}_{n,k}^\dagger \hat{L}_{n,k}, \cdot\} \right), \tag{S5}$$

with GKSL operators $\hat{L}_{n,k} \in \mathcal{B}(\mathcal{H}_n^S)$.

As a first approximation, we divide the total propagation into M short time steps δt and perform a second-order Suzuki-Trotter splitting [74] between the chain and the environment terms

$$e^{\mathcal{L}t} = \left[e^{\mathcal{L}\delta t} \right]^M \tag{S6}$$

$$\simeq \left[e^{\mathcal{L}_{\text{chain}} \frac{\delta t}{2}} e^{\left(\sum_n^N \mathcal{L}_n^E \delta t\right)} e^{\mathcal{L}_{\text{chain}} \frac{\delta t}{2}} \right]^M \tag{S7}$$

$$= \left[e^{\mathcal{L}_{\text{chain}} \frac{\delta t}{2}} \left(\prod_{n=1}^{N} e^{\mathcal{L}_n^E \delta t} \right) e^{\mathcal{L}_{\text{chain}} \frac{\delta t}{2}} \right]^M, \tag{S8}$$

where the last equality follows from the fact that the $\mathcal{L}_n^E$ act on disjoint spaces. For ease of presentation we now apply this propagator to a total initial state that is separable between the chain and each environment, i.e. $\rho(0) = \tilde{\rho}_{\text{chain}} \bigotimes_n \tilde{\rho}_n^E$. We comment below how this can be extended to initially correlated states. Let us now consider the reduced chain state, which we obtain by performing the partial traces over all environments, i.e. $\text{Tr}_E := \text{Tr}_{\{\bigotimes_n \mathcal{H}_n^E\}}$. Assuming an initial separable state and the approximated propagator from Eq. (S8), Fig. S1a expresses $\rho_{\text{chain}}(t) := \text{Tr}_E\, e^{\mathcal{L}t}\rho(0)$ as a tensor network for three time steps.

So far, the tensor network in Fig. S1a is unsuitable for carrying out a numerical computation. The tensors representing the interaction with the environment (red tensors) explicitly involve the environment Hilbert spaces, and the chain propagators $e^{\mathcal{L}_{\text{chain}} \frac{\delta t}{2}}$ (green tensors) are still assumed to be exact, with a total dimension of $\dim(\mathcal{H}_n^S)^{4N}$. This is impractical for any generic environment and any chain of significant length. In the following we present how to construct the tensor network in Fig. S1c instead, which is then suitable for an efficient numerical computation.

First, we consider the part of the tensor network that consists of the environment initial state $\tilde{\rho}_n^E$, the interaction propagators $e^{\mathcal{L}_n^E \delta t}$, and the final environment trace $\text{Tr}_{\mathcal{H}_n^E}$, which we draw again on the left hand side of Fig. S1b. Together, these tensors constitute a multilinear map, which is—per definition—the process tensor of the system-environment interaction Hamiltonian $\hat{H}_n^E$ for the initial state $\tilde{\rho}_n^E$ [36]. In principle each process tensor is of dimension $\dim(\mathcal{H}_n^S)^{4M}$, but in many cases can be efficiently represented by a matrix product operator (MPO) with a truncated bond dimension. This truncated bond dimension depends on the specific Hamiltonian $\hat{H}_n^E$ and can be understood as a measure of quantum non-Markovianity for the environment interaction

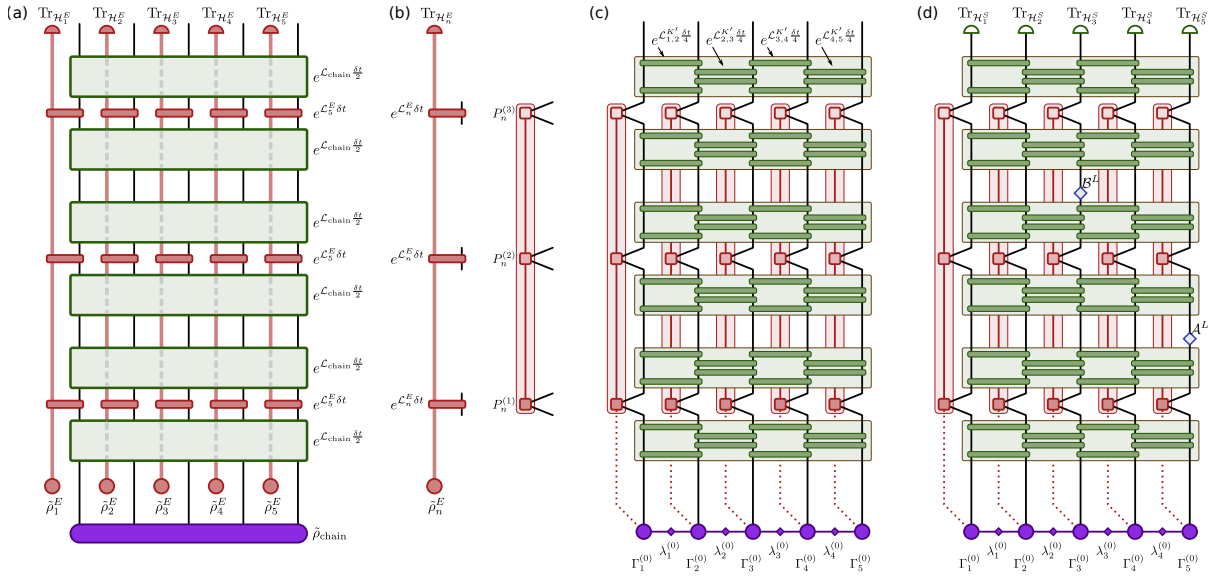

FIG. S1. Tensor networks combining process tensors and TEBD. (a) Tensor network for three time steps using a second-order Suzuki-Trotter splitting between a 5-site chain and its environments. (b) A process tensor (left hand side) and the corresponding PT-MPO (right hand side). (c) Full tensor network for a 5-site chain using a second order Suzuki-Trotter splitting in both environment and inter-site coupling. (d) Full tensor network to compute the two time correlation $\langle \hat{B}(2\delta t), \hat{A}(1\delta t)\rangle$.

at hand [49]. We have briefly described a few of the currently available methods for the computation of process tensors in MPO form (PT-MPO) for various environments [37–43] in the main text. The right hand side of Fig. S1b shows such a PT-MPO for three time steps. In Fig. S1c we have replaced the process tensors with the PT-MPOs obtained by one of the methods mentioned above. Given that the computation of such a PT-MPO is often numerically involved, it can be beneficial to absorb all pure on-site system terms into $\mathcal{L}_n^S$ and reuse the PT-MPO for any identical occurrences of the $\mathcal{L}_n^E$ environment interactions.

Next, we consider the chain propagators $e^{\mathcal{L}_{\text{chain}}\frac{\delta t}{2}}$. To decompose these large tensors into smaller tensors, we perform another second-order Suzuki-Trotter splitting (this time among the chain sites), making use of the fact that the chain Hamiltonian only contains on-site and nearest neighbor terms. Higher order expansions and long range couplings are also possible [72, 74]. This standard procedure leads to a TEBD tensor network for the chain evolution in Liouville space [34, 35]. For this, we first absorb the on-site system Hamiltonians $\hat{H}_n^S$ into the nearest neighbor terms $\hat{K}_{n,n+1}$ by defining

$$\hat{K}'_{n,n+1} := \hat{K}_{n,n+1} + \begin{cases} \hat{H}_1^S + \frac{1}{2}\hat{H}_2^S & \text{for } n = 1 \\ \frac{1}{2}\hat{H}_{N-1}^S + \hat{H}_N^S & \text{for } n = N-1 \\ \frac{1}{2}\hat{H}_n^S + \frac{1}{2}\hat{H}_{n+1}^S & \text{otherwise,} \end{cases} \tag{S9}$$

such that $\mathcal{L}_{\text{chain}} = \sum_{n=1}^{N-1} \mathcal{L}_{n,n+1}^{K'}$. A first-order Suzuki-Trotter splitting, for example, then yields

$$e^{\mathcal{L}_{\text{chain}}\frac{\delta t}{2}} = \exp\left(\sum_n \mathcal{L}_{n,n+1}^{K'}\frac{\delta t}{2}\right) \tag{S10}$$

$$= \exp\left(\sum_{n\,\text{odd}} \mathcal{L}_{n,n+1}^{K'}\frac{\delta t}{2} + \sum_{n\,\text{even}} \mathcal{L}_{n,n+1}^{K'}\frac{\delta t}{2}\right) \tag{S11}$$

$$\simeq \prod_{n\,\text{odd}} e^{\mathcal{L}_{n,n+1}^{K'}\frac{\delta t}{2}} \prod_{n\,\text{even}} e^{\mathcal{L}_{n,n+1}^{K'}\frac{\delta t}{2}}. \tag{S12}$$

In Fig. S1c we replace the half time step chain propagators $e^{\mathcal{L}_{\text{chain}}\frac{\delta t}{2}}$ with a second-order Suzuki-Trotter splitting, which is of a similar form as the first-order splitting presented in equation Eq. (S12) and consists of two body gates of the form $e^{\mathcal{L}_{n,n+1}^{K'}\frac{\delta t}{4}}$.

Finally, we insert the initial chain state as a matrix product state (MPS) in Vidal form [33]. Although the pure chain propagation works completely analogously to TEBD, each of the Γ tensors of the MPS needs to have an extra leg which corresponds to the entanglement of the chain site with its environment. We will call this MPS the *augmented MPS*. For initially uncorrelated chain-environment states the MPS has initially no such legs. In such cases, we nonetheless include dummy legs of dimension 1. These are indicated with dotted lines in Fig S1c. We do this such that the contraction algorithm for the first time step is of the same form as for all later steps, as well as to include the case of an initially correlated state [36], for which the dimension of the dotted lines is > 1.

Contraction algorithm.—Figure S1c shows the full tensor network for three time steps of a 5-site chain. To contract such a network we propose to absorb the tensors into the augmented MPS line by line. This involves two different types of contraction sequences which we describe in the following.

The first type is a contraction of the augmented MPS with the chain propagators, which consist of two-site nearest neighbor gates. We suggest a sequence of operations in Figs. S2(c-h). Compared to the canonical TEBD, this sequence includes some additional operations for the augmented legs with the aim of minimizing the size of the intermediate tensors involved. Figures S2(c-h) show the proposed operations for applying a two body gate $G = e^{\mathcal{L}^{K'}_{n,n+1}\frac{\delta t}{4}}$ to an augmented MPS:

(c-d) Contraction:
$B_L := \lambda_{n-1}\Gamma_n$ and $B_R := \Gamma_{n+1}\lambda_{n+1}$

(d-e) Truncated singular value decomposition:
$U^B_L \Sigma^B_L V^{\dagger B}_L :\simeq B_L$ and $U^B_R \Sigma^B_R V^{\dagger B}_R :\simeq B_R$

(e-f) Contraction:
$D := \Sigma^B_L\, V^{\dagger B}_L\, \lambda_n\, G\, U^B_R\, \Sigma^B_R$

(f-g) Truncated singular value decomposition:
$U^D \Sigma^D V^{\dagger D} :\simeq D$ and $\tilde{\lambda}_n := \Sigma^D$

(g) Insert identities:
$\lambda_{n-1}\lambda^{-1}_{n-1} = \mathbb{1}$ and $\lambda^{-1}_{n+1}\lambda_{n+1} = \mathbb{1}$

(g-h) Contraction:
$\tilde{\Gamma}_n := \lambda^{-1}_{n-1} U^B_L U^D$ and $\tilde{\Gamma}_{n+1} := V^{\dagger D} V^{\dagger B}_R \lambda^{-1}_{n+1}$

We use a relative singular value truncation threshold ϵ, which we typically set to be of the order 10^{-6}. Let $\tilde{U}\tilde{\Sigma}\tilde{V}^\dagger = X$ be an exact singular value decomposition of the matrix $X \in \mathbb{C}^{a\times b}$. We then choose the truncated bond dimension χ to be as small as possible, while maintaining $\left\|\tilde{\Sigma} - \Sigma\right\|_2 < \epsilon \max[\tilde{\Sigma}]$. Here, $U \in \mathbb{C}^{a\times\chi}$, $\Sigma \in \mathbb{C}^{\chi\times\chi}$, and $V^\dagger \in \mathbb{C}^{\chi\times b}$ denote the truncated matrices and $\left\|\tilde{\Sigma} - \Sigma\right\|_2$ is the 2-norm of the discarded singular values.

The other type of operation that occurs when absorbing the tensor network line by line is the contraction of the augmented MPS with the subsequent parts of the PT-MPOs. Figures S2(i-j) show the contraction of an augmented MPS site (Γ_n) with a single tensor of a PT-MPO (P_n). This contraction only updates the Γ tensors of the augmented MPS, where the bond legs of the PT-MPOs become the new augmented legs of the augmented MPS.

We point out that the contraction sequences described above only act locally on a short part of the augmented MPS for each step. This contraction scheme is therefore well suited for parallel computing.

Intermediate chain evolution.—As presented thus far, this method would only yield a reduced chain state at the final time step. We can, however, extract the reduced density matrix of the chain for every intermediate time step by temporarily removing the correlations of the augmented MPS with the environment. This can be done using the so called *containment* property of process tensors, which allows the generation of process tensors for a smaller set of time slots by tracing over all later time slots [36]. For this we construct the tensors $C^{(m)}_n$ (which we call *cap* tensors) as shown in Figs. S2(a-b). Applying these cap tensors to the augmented MPS at time step m removes the augmented leg and yields a canonical MPS that represents the vectorized reduced density matrix of the chain at that time (see Figs. S2(k-l)).

Multi-site multi-time correlations.—Finally, we explain how to compute multi-site multi-time correlations. As an example, we could be interested in the correlation $\langle \hat{B}(2\delta t), \hat{A}(1\delta t)\rangle$, with $\hat{A}$ and $\hat{B}$ acting on the 5$^{\text{th}}$ and 3$^{\text{rd}}$ spin of a 5-site chain respectively. More generally, we consider all correlations C of the form

$$C = \langle \prod_{p=1}^{P} \hat{C}_p(m_p\delta t)\rangle, \tag{S13}$$

with P time-ordered operators acting on possibly different chain sites $\hat{C}_p \in \mathcal{B}(\mathcal{H}^S_{n_p})$ at times $m_p\delta t$. This can be written as

$$C = \mathrm{Tr}\left[\prod_{p=1}^{P}\left(\mathcal{C}^L_p\, e^{\mathcal{L}(m_p - m_{p-1})\delta t}\right)\rho(0)\right] \tag{S14}$$

$$= \mathrm{Tr}\left[\prod_{p=1}^{P}\left(\mathcal{C}^L_p[\, e^{\mathcal{L}\delta t}]^{(m_p - m_{p-1})}\right)\rho(0)\right], \tag{S15}$$

with $m_0 := 0$ and the left acting super-operators $\mathcal{C}^L_p := \hat{C}_p\,\cdot$. To represent Eq. (S15) as a tensor network, we replace the full propagators $e^{\mathcal{L}\delta t}$ with the same construction as above. This leads to the same tensor network as in Fig. S1c, but with additionally inserted super-operators and with additional traces over the chain sites at the top of the network. We exemplify this in Fig. S1d for the above example of $\langle \hat{B}(2\delta t), \hat{A}(1\delta t)\rangle$. Finally, we mention that for out-of-time ordered correlations, the operators need to be inserted as right acting super-operators $\mathcal{C}^R_p := \cdot\, \hat{C}_p$ instead.

An XYZ spin chain with thermal leads

In this section we present further details and results of the spin chain simulations discussed in the main text. We comment on the process tensor computation and explain how we use the PT-MPO approach to TEBD introduced in the previous section to compute the fluctuation and dissipation spectra. In the two subsections that follow

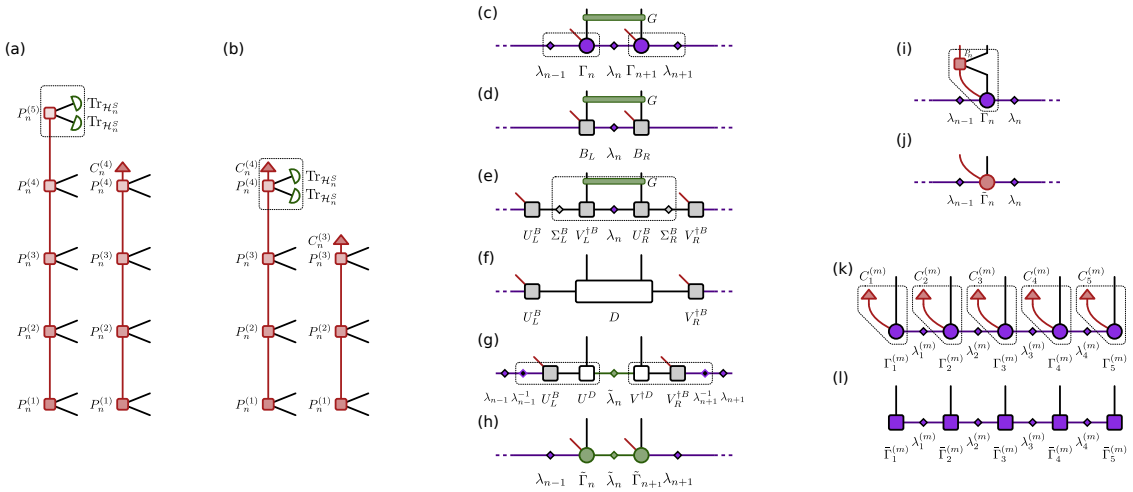

FIG. S2. Contraction algorithms for the PT-MPO and augmented MPS. (a) Construction of the 4^{th} cap tensor $C_n^{(4)}$ of the PT-MPO at site n. (b) Construction of the 3^{rd} cap tensor $C_n^{(3)}$. (c-h) Contraction and decomposition sequence for the application of a two-site gate G on the augmented MPS. (i-j) Contraction of the augmented MPS with a PT-MPO tensor. (k-l) Contraction of the augmented MPS with the cap tensors, yielding a canonical MPS in Liouville space.

we present further results and simulation details for the 5-site spin chain coupled to a single bath and the 9-site spin chain placed between a hot and a cold bath.

Process tensor computation.—The method introduced above requires pre-computed PT-MPOs to capture the interactions with the environments. We consider bosonic baths with an Ohmic spectral density, coupling strength of $\alpha = 0.32$, and a cutoff frequency $\omega_c = 4.0$ (see Eq. (3) and the text following). A suitable method for the computation of the corresponding PT-MPO is the a process tensor adoption of the time evolving matrix product operator (PT-TEMPO) method [37–40]. Such a computation has three convergence parameters: the time step δt, the maximal number of memory steps $\Delta K_{\max}$, and the relative singular value truncation threshold ϵ_{TEMPO}. The product $\delta t\, \Delta K_{\max}$ is the maximal correlation time of the environment that is included in the computation. The environment correlation function

$$C(\tau) = \int_0^\infty J(\omega) \left[\cos(\omega\tau) \coth\left(\frac{\omega}{2T}\right) - i \sin(\omega\tau)\right] \mathrm{d}\omega \tag{S16}$$

drops at time $t = 8.0$ below 10^{-3} of its maximum value. Consistent with this, we find the choice of $\delta t = 0.2$, $\Delta K_{\max} = 40$, and $\epsilon_{\text{TEMPO}} = 10^{-6}$ to be adequate. We comment on checking the convergence of the simulations in more detail further below. We carried out the computation of the PT-MPOs using the open source package [40]. It took approximately 4 minutes to calculate a process tensor with 1600 time steps on a single core of an Intel i7 (8th Gen) processor. The resulting process tensors have a maximal bond dimension of 37 and 44 for the temperatures $T_{\text{hot}} = 1.6$ and $T_{\text{cold}} = 0.8$ respectively.

Fluctuation and dissipation spectra.—To extract dissipation and fluctuation spectra we first evolve the spin chain from the initial state at time $t_i = 0.0$ to the approximate steady state at time t_{ss}. During the TEBD propagation we used a relative singular value truncation of $\epsilon_{\text{TEBD}} = 10^{-6}$. We found that for all scenarios considered, $t_{ss} = 192.0$ (960 steps) is long enough to reach an approximate steady state. For the results presented in this Letter we have chosen the initial state of each spin to be $\tilde{\rho}_n^S \propto \exp\left(\frac{\hat{\sigma}^z}{2T_n}\right)$ where $T_n = T_{\text{hot}}$ and $T_n = T_{\text{hot}} + \frac{n-1}{8}(T_{\text{cold}} - T_{\text{hot}})$ for the 5-site and the 9-site chains respectively. As expected, we found the same steady state and the same two-time correlations when starting from other random initial product states.

Then, to compute two-time correlations such as $\langle \hat{B}(t_{ss}+\tau)\hat{A}(t_{ss})\rangle$ with respect to some single site operators $\hat{A}$ and $\hat{B}$, we apply the left acting super-operator $\mathcal{A}^L = \hat{A}\cdot$ to the steady state and compute the expectation value of $\hat{B}$ for all later times up to the final time $t_f = 320.0$. We can thus compute the two time correlations $\langle \hat{\sigma}_n^z(t_{ss}+\tau)\hat{\sigma}_n^z(t_{ss})\rangle$ of spin n for all τ up to $\tau_{\max} := t_f - t_{ss}$ with a single propagation starting from the steady state. It is important to point out that the expression "steady state" refers to the state of the whole (chain and environments) and not just the reduced chain state. Because the two-time auto-correlations of the chain depend on the steady state correlations of the chain with the environment, it is vital to continue the propagation from the full augmented MPS, incorporating entanglement with the environment, at time t_{ss}.

With this, we obtain $\langle \hat{\sigma}_n^z(t_{ss}+\tau)\hat{\sigma}_n^z(t_{ss})\rangle$ for all $\tau \in (0, \tau_{\max})$, which we identify with $\langle \hat{\sigma}_n^z(\tau)\hat{\sigma}_n^z(0)\rangle_{ss}$ at

the steady state. Using

$$\langle \hat{\sigma}_n^z(\tau)\hat{\sigma}_n^z(0)\rangle_{ss} = \langle \hat{\sigma}_n^z(0)\hat{\sigma}_n^z(-\tau)\rangle_{ss} \quad \text{(S17)}$$
$$= \langle \hat{\sigma}_n^z(0)\hat{\sigma}_n^z(\tau)\rangle_{ss}^* \quad \text{(S18)}$$

we can construct commutators and anti-commutators for $\tau \in (-\tau_{\max}, \tau_{\max})$ and employ a fast Fourier transformation on this interval to compute the fluctuation and dissipation spectra.

In order to check the convergence of the simulations with respect to the computation parameters, we study the finite differences of our results with respect to altered parameters. We performed simulations substituting $\delta t = 0.2 \to 0.15$, $\Delta K_{\max} = 40 \to 30$, $\epsilon_{\text{TEMPO}} = 10^{-6} \to 10^{-5}$ for the process tensor computation; and $\epsilon_{\text{TEBD}} = 10^{-6} \to 10^{-5}$, $t_{ss} = 192.0 \to 160.0$, and $\tau_{\max} = 128.0 \to 160.0$ for the augmented TEBD evolution. We found that the resulting differences are dominated by the variation of ϵ_{TEBD} and we thus use these differences as an estimate for the numerical error. We plot this error estimate in Figs. 3(b) and 3(d) as shaded regions. For all other plots (see Figs. 2, S4, and S5) the estimated error is smaller or similar to the thickness of the lines.

We carried out all computations using Python3 code that will be made public soon as part of an open source package [40]. The total propagation for the single bath 5-site chain took 68 minutes on a single core of an Intel i7 (8th Gen) machine. For the 9-site chain the propagation from the initial state to the steady state took 8 hours 6 minutes on four cores of an Intel Xeon E5-2695 machine. The propagation after the application of the first $\hat{\sigma}_n^z$ took between 6 hours 37 minutes and 8 hours 39 minutes, depending on the site n to which it was applied.

Spin chain coupled to a single bath

In this subsection we present further details and results for the 5-site spin chain coupled to a single bath. We consider the chain Hamiltonian specified in the main text in Eq. (2) with $N = 5$ and couple a single thermal bath at temperature $T = T_{\text{hot}} = 1.6$ to the first site. We study this scenario for various coupling strengths to confirm that the steady state approaches the thermal Gibbs state of the closed chain in a weak coupling limit. Also, we briefly explain the two-spin GKSL driving method, which was used for comparison in Fig. 2 in the main text.

Single bath weak coupling limit.—Perturbation theory predicts that in a weak coupling limit the reduced chain density matrix of the full thermal state differs from the Gibbs state of the chain Hamiltonian at a quadratic order in the bath coupling [24]. The dimensionless coupling strength α is proportional to the square of the bath coupling amplitudes $|g_k|^2$, i.e. $\alpha \propto \sum_k |g_k|^2$. Assuming that the chain thermalizes with the bath in the long time limit, we thus expect to find a difference between the reduced steady state and the Gibbs state of the chain Hamiltonian that is proportional to α in a weak coupling limit. Figure S3 shows the trace distance for various coupling strengths α. A fit to the data shows that the results are consistent with the expectation.

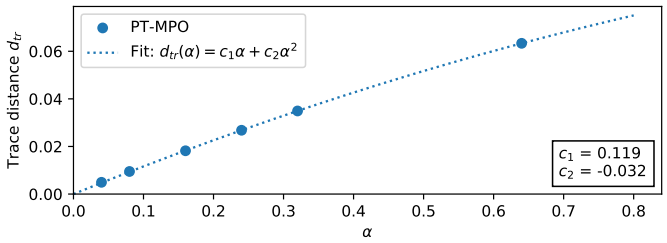

FIG. S3. Trace distance between the thermal Gibbs state of the closed 5-site spin chain and the approximate steady state of the chain coupled to the bath with varying coupling strength α. A fit shows that this difference is vanishing at a linear order in α (i.e. a quadratic order in bath couplings g_k) in a weak coupling limit.

Two-spin GKSL driving.—To compute the dashed lines in Fig. 2 in the main text we employed the two-spin bath protocol introduced in [63]. For this we attach two additional spins (at positions $n = -1$ and $n = 0$) to the left hand side of the first spin and construct a Liouvillian $\mathcal{L}_B$ which drives these two spins towards the Gibbs state of their local Hamiltonian as described in section 2.4 of reference [63]. Because the augmented TEBD method reduces to the canonical TEBD in Liouville space when no PT-MPOs are added to the network, we can use the exact same approach and implementation as described above. For this, we simply do not attach any PT-MPO to the network, and instead substitute $\mathcal{L}_{-1,0}^{K'} \to \mathcal{L}_{-1,0}^{K'} + \mathcal{L}_B$ to include the time local driving terms.

Spin chain placed between a hot and a cold bath

In this subsection we present further details and results for the 9-site spin chain placed between a hot and a cold bath. We consider the chain Hamiltonian specified in the main text in Eq. (2) with $N = 9$ and couple one bath at temperature $T_{\text{hot}} = 1.6$ to the first site and one bath at temperature $T_{\text{cold}} = 0.8$ to the last site. We present the dissipation spectra and the effective temperature with respect to the $\hat{\sigma}^x$ and $\hat{\sigma}^y$ observables and plot the bond dimension during the propagation of the augmented MPS for these simulations. Finally, we present the density of states for the closed chain (i.e. without any environment) for comparison.

Results for $\hat{\sigma}^x$ and $\hat{\sigma}^y$.—Figures S4 and S5 show the dissipation spectra and the effective temperature with respect to the observables $\hat{\sigma}^x$ and $\hat{\sigma}^y$, and thus com-

plement Fig. 3 from the main text. In all three figures we used the same on-site disorder $\epsilon_n = 1 + x_n$ with $x_n = (0.16, 0.69, 0.33, 0.14, -0.24, 0.47, -0.20, 1.25, 1.48)$ for the results shown in the right column. The effective temperature plots in Figs. S4(b) and S5(b) do not show the distinct low, mid, and high frequency regions as in Fig. 3(b). However, the results are still consistent with the explanation suggested in the main text. For the clean chain (without disorder), the inner spins tend to assume a collective common temperature at frequencies where their density of states is larger than the density of states for the outer spins. Conversely, at higher frequencies where the density of states of the outer spins is dominant, the surface states have an increased influence, and the effective temperature is more spread out.

Augmented MPS bond dimensions.—Figure S6 shows the bond dimensions of the augmented MPS during the propagation of the spin chain from the initial to the approximate steady state. As expected, the bond dimension is larger towards the middle of the chain. It appears that the transient dynamics of the chain passes through a state with a significantly higher entanglement entropy among the sites compared to the steady state, signaled by the bond dimension peak at about $t = 8.0$. Panel (c) of Fig. S7 shows the the maximal bond dimension of the augmented MPS as a function of time after the application of $\hat{\sigma}^z_n$ for each site n of the clean spin chain. It shows a similar behavior to the bond dimension during the initial propagation and peaks at approximately $\tau = 7.0$. In Figs. S7(a) and S7(b) we observe a plateau at its highest value before it drops towards the end of the simulation.

Density of states of the closed spin chain.—Figure S8 shows the density of states with respect to $\hat{\sigma}^x$, $\hat{\sigma}^y$, and $\hat{\sigma}^z$ for the closed spin chain at an intermediate temperature of $T_{\text{mid}} = 1.2$. We obtained these results from exact diagonalization and included a line broadening with a Lorentzian shape for each mode (with a width of 0.1) in order to approximate the effect of the environment. As mentioned in the main text, we can see that for the clean spin chain the density of states with respect to $\hat{\sigma}^z$ slowly vanishes above a frequency of approximately 2.5. In contrast, for the operators $\hat{\sigma}^{x,y}$ we see the density of states extend to higher frequencies. This is because these operators couple spaces with different values of $\sum_n \hat{s}^z_n$, and the energies of these states are split by the on-site field ϵ_n.

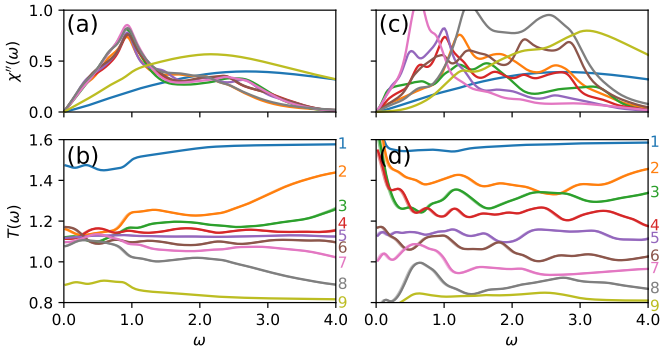

FIG. S4. The dissipation spectrum (a) and effective temperature (b) at steady state for the $\hat{\sigma}^x$ observable of each spin in a 9-site spin chain placed between a hot ($T_{\text{hot}} = 1.6$) and cold bath ($T_{\text{cold}} = 0.8$). Panels (c) and (d) show the results for the same chain with additional on-site disorder.

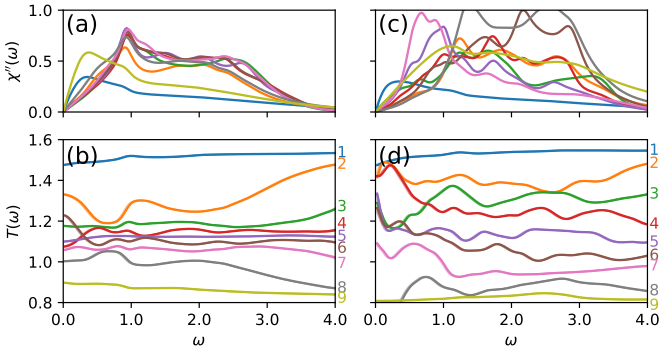

FIG. S5. The dissipation spectrum (a) and effective temperature (b) at steady state for the $\hat{\sigma}^y$ observable of each spin in a 9-site spin chain placed between a hot ($T_{\text{hot}} = 1.6$) and cold bath ($T_{\text{cold}} = 0.8$). Panels (c) and (d) show the results for the same chain with additional on-site disorder.

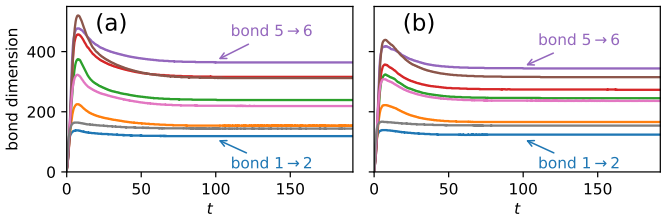

FIG. S6. The bond dimensions of the augmented MPS during the propagation of the 9-site spin chain placed between two baths from the initial to the approximate steady state, for the clean (a) and disordered case (b).

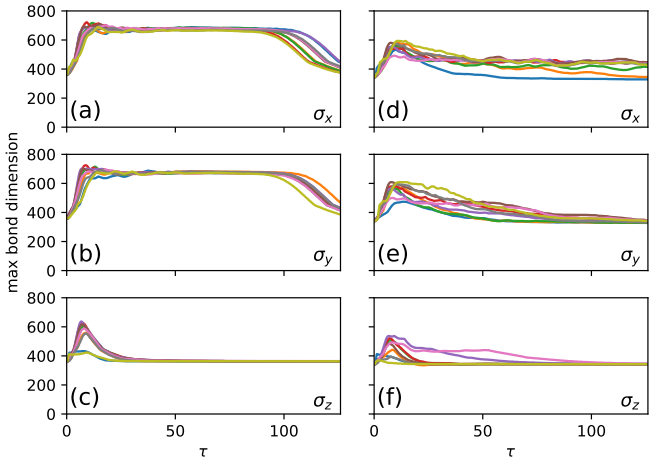

FIG. S7. The maximal bond dimension of the 9-site spin chain augmented MPS as a function of time after the application of $\hat{\sigma}_n^x$, $\hat{\sigma}_n^y$, and $\hat{\sigma}_n^z$ for each site n and the clean (a-c) and disordered case (d-f).

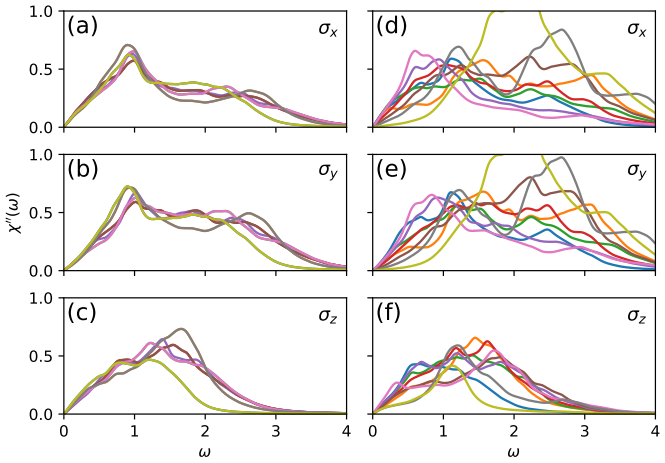

FIG. S8. Density of states $\chi''(\omega)$ for the closed 9-site spin chain with respect to $\hat{\sigma}_n^x$, $\hat{\sigma}_n^y$, and $\hat{\sigma}_n^z$ for each site n, and the clean (a-c) and disordered case (d-f).